Thomas, C., Igel, H., Weber, M., Scherbaum, F. (2000): Acoustic simulation of P-wave propagation in a heterogeneous spherical earth: numerical method and application to precursor waves to PKPdf. - Geophysical Journal International, 141, 2, pp. 307—320.

DOI: https://doi.org/10.1046/j.1365-246x.2000.00079.x

*Geophys. J. Int.* (2000) **141,** 307–320

# Acoustic simulation of *P*-wave propagation in a heterogeneous spherical earth: numerical method and application to precursor waves to *PKPdf*

Ch. Thomas,[1,*] H. Igel,[2,†] M. Weber[3] and F. Scherbaum[4]

[1] *Institut für Geophysik, Göttingen, Germany*
[2] *Institute of Theoretical Geophysics, Cambridge, UK*
[3] *GeoForschungsZentrum Potsdam, Potsdam, Germany*
[4] *Universität Potsdam, Potsdam, Germany*

Accepted 1999 November 15. Received 1999 October 21; in original form 1999 February 4

## SUMMARY

To be able to simulate *P*-wave propagation in a heterogeneous spherical earth, we solve the acoustic wave equation in spherical coordinates numerically for axisymmetric media. We employ a high-order finite difference scheme that allows us to simulate arbitrary heterogeneous structures with wavelengths as small as 10 km. A standard regular gridding in spherical coordinates leads to a continuously decreasing effective grid increment towards the earth's centre. To avoid the resulting stability problems, we regrid the lateral domain several times, thereby drastically improving the stability criterion for whole earth models. Treatment of the earth's centre in a Cartesian system allows us to model wave propagation through the centre of the earth. We present the algorithm in the acoustic approximation and show its applicability to simulate whole-earth *P*-wave propagation. In the present implementation, wavefields with a dominant period of about 10 s can be simulated. As an application, we investigate, in a parameter study, the influence of scatterers in the earth's lower mantle on core phases (*PKP*). Scatterers with various velocity contrasts (up to $\pm 30$ per cent) have been placed at different locations in the lower mantle to study their effects on the *PKP* wavefield. The location and the velocity contrast of a scatterer affect the amplitude, the slowness of the scattered phase and its traveltime. In addition to individual scatterers, we also study models with two and more scatterers with different orientations. It is shown that—for the frequency range considered—the difference between a scatterer at the CMB and a scatterer 500 km above the CMB is small. In addition, a global ultra-high-velocity layer and an ultra-low-velocity layer have been placed at the bottom of the mantle, but it turns out that they are not able to produce arrivals in the time window where precursors are usually expected. We demonstrate the advantages of vespagram analysis to distinguish between different scatterer mechanisms, locations of scatterers and diffracted waves from the caustic at 144°.

**Key words:** body waves, core phases, finite differences, scattering, seismic wave propagation, spherical earth.

## 1 INTRODUCTION

One of the main goals of seismology today is a detailed understanding of the 3-D heterogeneities inside the Earth on a global scale. In the past years tomographic inversion of long-period seismic waveforms and arrival times have provided us with more and more detailed images of long-wavelength heterogeneities inside the mantle, giving us insight into the state of the Earth's convective system. However, to answer some of the fundamental questions relating to the dynamics and fate of subducting plates or the uprising of hot material through hotspots, a more detailed understanding of the small-scale structure is required. To achieve this, an understanding of 3-D wave propagation including all waveform effects on a global scale is crucial.

* Now at: School of Earth Sciences, University of Leeds, Leeds, LS2 9JT, UK. E-mail: t.thomas@earth.leeds.ac.uk
† Now at: Institut für Allgemeine und Angewandte Geophysik, Ludwig-Maximilians Universität, München, Germany.

The calculation of complete synthetic seismograms for 3-D global structures has to be undertaken by numerical means. The normal mode approach to the general problem seems inappropriate for the sharp lateral contrasts that are likely to exist in the upper mantle, because of the enormous amount of modes that would have to be coupled. Several attempts have been made to develop numerical algorithms for global wave propagation. Following the early work by Alterman *et al.* (1970), finite difference (FD) approximations to rotationally symmetric media were developed by Igel & Weber (1995, 1996), Igel & Gudmundsson (1997) and Chaljub & Tarantola (1997). Furumura *et al.* (1998) presented a pseudospectral method that attempted to simulate global seismograms with a cylindrical approximation. The Direct Solution Method (Geller & Ohminato 1994), first developed for spherically symmetric media (Cummins *et al.* 1994a,b), has been extended to (long-wavelength) laterally varying structures (Cummins *et al.* 1997). 3-D algorithms for spherical media were suggested by Yoon & McMechan (1995) and Igel (1999), but it is obvious that they will be restricted to long-period wave propagation for some time to come due to the enormous computational costs. For this reason, the axisymmetric approximation has proved to be of considerable potential because the effects of heterogeneities can be studied at high frequencies (Chaljub & Tarantola 1997; Igel & Ita 1997).

In the axisymmetric problem in spherical coordinates, several difficulties occur: (1) the sources also have to be axisymmetric, which at present limits the source types to toroidal sources (*SH* motion), explosions or vertical forces (*P–SV* motion); (2) for regular lateral grid spacing the lateral grid increment decreases with depth, forcing unrealistically small time steps in time-dependent calculations through the stability criterion for models with large depth range; (3) in the *P–SV* case—if we want to model global wave propagation—we have to include the Earth's centre, which is a singularity in spherical coordinates.

In this paper we present an approach to overcome the latter two of these difficulties. We describe the algorithm in the acoustic approximation. Whilst this approximation is not appropriate for the simulation of the Earth's elastic wavefield, it is still useful for studies of primary (*P*) arrivals and the effects of heterogeneities on them. The advantage is that because of the reduced size of the problem, higher frequencies can be achieved.

We employ a multidomain approach with variable grid increments that allows us to carry out whole Earth *P*-wave simulations for laterally heterogeneous media in a spherical system. An extension of this approach to the elastic case is in progress.

As an application we use this algorithm to simulate and model precursors to the *PKPdf* phase. Precursors to *PKPdf* (a wave that travels through the inner core) have long been discussed as scattered waves from inhomogeneities in the lower mantle or at the core–mantle boundary. Cleary & Haddon (1972), Haddon & Cleary (1974), Doornbos & Vlaar (1973) and King *et al.* (1973) showed with array methods that the phases ahead of *PKPdf* originate from the scattering of *PKP* at small inhomogeneities in the lowermost 200 km of the Earth's mantle ($D''$ region) at either the source side (where the wave enters the core) or the receiver side (where the wave exits the core). For source-side scattering the scatterer has to be on the *PKPdf* path, whereas receiver-side scattering requires a scatterer on the *PKPab* path (e.g. Doornbos & Vlaar 1973; see also Fig. 1). From looking at stacks of global data containing precursors to *PKPdf*, Hedlin *et al.* (1997) argued that the origin of the scattered waves can be small-scale inhomogeneities with a weak velocity contrast (1–2 per cent) throughout the whole mantle. In contrast, Vidale & Hedlin (1998) found that scattering from South Pacific events recorded in Norway took place only in the lowest 60 km of the mantle. They determined the rms velocity contrast of the scatterers to be between 10 and 15 per cent and therefore concluded that the scattered waves result from melt at the base of the mantle. More recent work (Wen & Helmberger 1998a), using long-period data and synthetics, showed that scatterers are located at the bottom of the mantle using a similar source–receiver combination. In their data they found long-period scattered phases that interfere with the diffracted *PKP* wave ($PKP_{\mathrm{diff}}$) from the B-caustic and are visible in single traces. The horizontal and vertical length scales of the scatterers were determined to be 100–300 km and 60–80 km, respectively, comparable to the size of the scatterers presented in our study. The *P*-velocity contrast has to be more than 7 per cent to explain the observations. Thomas *et al.* (1999) showed that it is possible to locate isolated scatterers in the lower mantle.

In a parameter study we investigate the influence of different scatterers in the $D''$ region on the *PKP* wavefield. Scatterers with various velocity contrasts compared to a reference earth model have been placed at different locations in the lower mantle and difference effects between these models have been studied.

Although the dominant periods used here (11 s) are much longer than the typical dominant periods of precursors observed in most studies (3–1 s), the effect of different velocity contrasts as well as different locations and orientations of scatterers can still be investigated. Moreover, long-period scattered waves have been found recently (Wen & Helmberger 1998a), as mentioned above.

## 2 THEORY

We denote $\sigma$ the pressure, $\rho$ the mass density and $u_r$ and $u_\theta$ the displacement components. The equations of motion in spherical coordinates $\{r, \theta, \varphi\}$ for axisymmetric media and sources are

$$\rho\partial_t^2 u_r = \partial_r(\sigma + p),$$

$$\rho\partial_t^2 u_\theta = \frac{1}{r}\,\partial_\theta(\sigma + p), \tag{1}$$

where $p$ is a pressure source, time and space dependence being implicit. The pressure is given by

$$\sigma = \lambda(\epsilon_{rr} + \epsilon_{\theta\theta} + \epsilon_{\varphi\varphi}), \tag{2}$$

where $\lambda$ is the Lamé parameter and the strain elements are

$$\epsilon_{rr} = \partial_r u_r, \tag{3}$$

$$\epsilon_{\theta\theta} = \frac{1}{r}\,(\partial_\theta u_\theta + u_r), \tag{4}$$

$$\epsilon_{\varphi\varphi} = \frac{1}{r}\,(u_r + \cot\theta u_\theta), \tag{5}$$

and $\partial_t$ denotes differentiation with respect to time (or space coordinates).

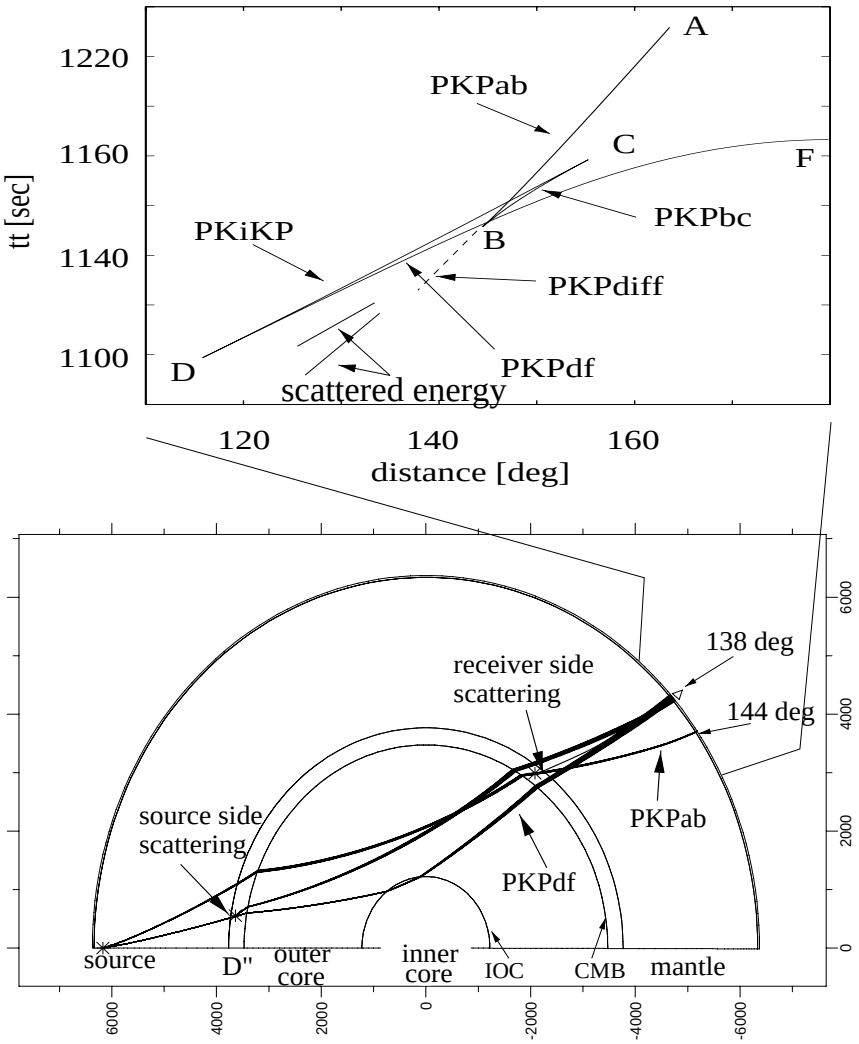


**Figure 1.** A cartoon of ray paths through the earth's core with scattering at the source and the receiver side, respectively, together with the main phases *PKPdf* and *PKPab* (bottom). For simplicity, *PKiKP* (the reflection at the inner core boundary, IOC) is not drawn. A traveltime curve for *PKP* and the scattered phases is also shown (top).

Whilst it may seem unusual to write the acoustic wave equation in this way, this is our choice to facilitate the extension to the fully elastic case. The same grid staggering (see below) can then be used as a starting point, and $\sigma$ will become the stress tensor. Note that these equations are not defined along the axis $\theta = 0$, $\pi$ and at $r = 0$. Special treatment of these domains will have to be applied when solving these equations numerically.

## 3 SPHERICAL GRID, STAGGERING AND STABILITY

All space-dependent fields are defined on a staggered grid shown schematically in Fig. 2. With a regular discretization of the $\theta$-domain, the arc length of the grid increment would become smaller and smaller towards the centre of the earth. Our aim is to be able to model whole-earth wave propagation, in particular core phases such as *PKP*. In FD calculations the time increment $dt$ has to be chosen in accordance with a stability criterion of the form

$$c \frac{\partial t}{\partial x} \leq \epsilon, \tag{6}$$

where $c$ is the (maximum) velocity in the medium, $dx$ is the grid increment and $\epsilon$ is some value ($\approx 1$) that can be calculated analytically or determined numerically. In a Cartesian grid the stability criterion in a homogeneous medium is constant everywhere. This is not the case in spherical coordinates, where the effective lateral grid increment (arc length) varies with depth. Since the grid distance is in the denominator of eq. (6), the time step required for a stable numerical calculation becomes smaller and smaller the greater the depth range of the physical domain. In addition, inside the earth's mantle the velocities increase with greater depth, further enhancing this effect.

To overcome these problems we introduce depth-dependent lateral grid spacing. Every time the arclength of the lateral grid increment decreases by a factor of two, the lateral grid spacing

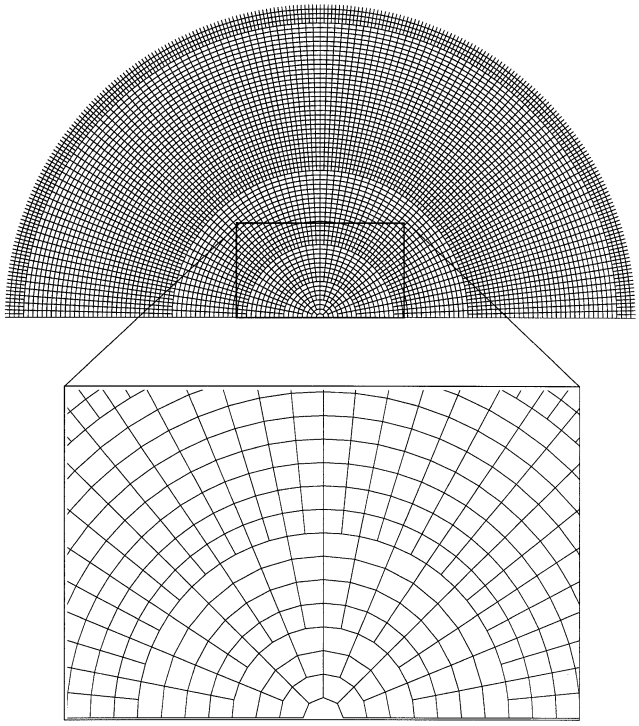

**Figure 2.** Physical domain for axisymmetric simulations. The angular range in $\theta$ is 180°. The lateral grid spacing is increased each time the arc length is halved. In our numerical examples we have eight domains. At the centre of the earth we use Cartesian coordinates.

is doubled (Fig. 2). The grid spacing is altered several times until the minimum radius of the innermost layer is so small that the earth's centre can be represented by a single grid cell. There, only the stress (pressure) is defined, which can be calculated in a Cartesian system from the radial displacements known on the spherical grid surrounding the centre (see below). The radial grid spacing is constant throughout the earth. The grid is also refined near the earth's surface. This improves the accuracy of the free-surface boundary condition at little extra computational cost (Igel & Gudmundsson 1997).

Variable grid spacing has previously been applied to finite difference wave propagation in media with strong velocity contrasts to avoid oversampling of the wavefield (e.g. Mozco 1989; Jastram & Behle 1992; Kessler & Kosloff 1993; Jastram & Tessmer 1994; Falk *et al.* 1996).

The effect of the multidomain approach on the grid increment is illustrated in Fig. 3. For example, if we want to simulate wave propagation down to 6000 km depth, the lateral grid spacing would decrease by a factor of $\approx 20$. By regridding we decrease the increment by less than a factor of two. Since the grid distance is linked to the required time step through eq. (6), the problem can be solved 10 times faster than without regridding. A further improvement is the gain in storage because of the lower grid density in the multidomain approach towards the centre.

Fig. 4 illustrates the staggering of the fields and the connection between two domains with different lateral grid spacing. At the bottom (top) of each domain some of the elements need to be interpolated to continue the vertical derivatives of the fields across the domain boundaries. This connection is carried out with second-order interpolation and derivative operators. Inside the domains the space derivatives are calculated with high-order (eight-point) operators. The same staggering can be used in the elastic case, where additional stress and strain elements will have to be added in the appropriate locations. The space and time operators used are described for a Cartesian algorithm in Igel *et al.* (1995). The implementation of sources in spherical grids is described by Igel & Gudmundsson (1997).

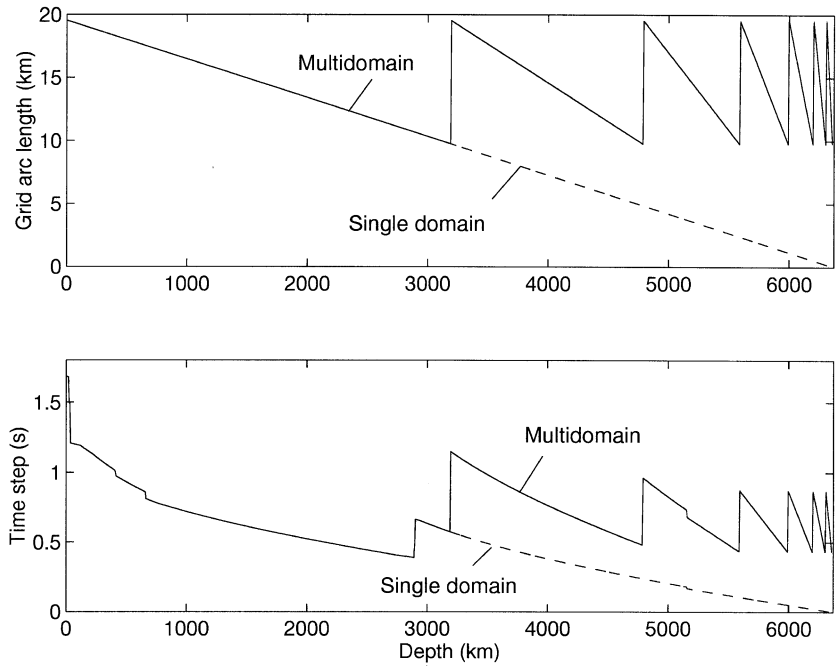


**Figure 3.** Top: arc length of grid increment as a function of depth with (solid) and without (dashed) the multidomain approach. Bottom: depth-dependent maximum required time step for a stable numerical simulation (according to eq. 6) for PREM (lateral size of top grid is 1024 gridpoints) with (solid) and without (dashed) varying the grid spacing.

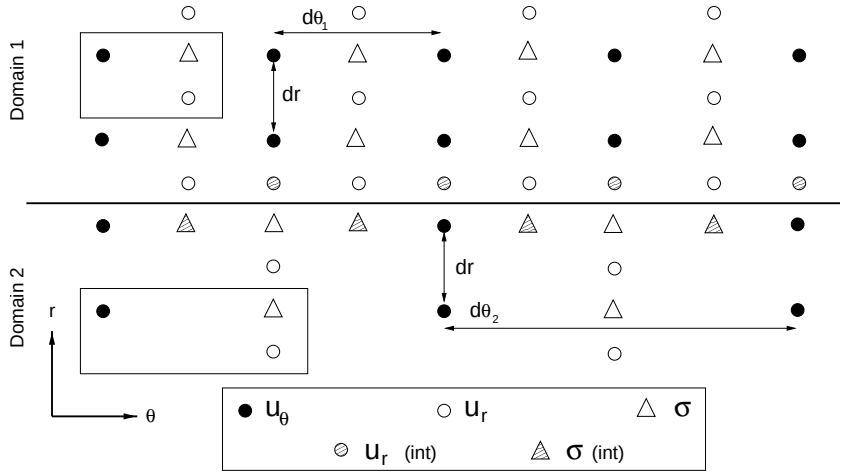


**Figure 4.** Staggered grid and domain connection. All fields are defined on a staggered grid. At the domain boundaries, where the lateral grid spacing is increased, some fields have to be interpolated (dashed symbols) to connect the domains. At the boundaries a second-order approach for the derivatives and the interpolation is applied. Inside the domains we use high-order operators for the space derivatives. The lateral grid spacing changes from $d\theta_1$ to $d\theta_2$ across the domain boundary (horizontal line), while the radial grid spacing $dr$ remains constant.

The treatment of the earth's centre is illustrated in Fig. 5. The grid was chosen in a way that at $r=0$ only the stress (pressure) is defined. Ignoring the fact that we are in a spherical system we can calculate the stress in Cartesian form using the radial displacements known at (or in this case interpolated to) $\theta=0$, $\pi/2$, and $\pi$:

$$\sigma=\lambda(\partial_x u_x+\partial_y u_y+\partial_z u_z)\,, \tag{7}$$

$$\sigma\approx(u_r^0+u_r^\pi+4u_r^{\pi/2})/dr_c\,, \tag{8}$$

where axisymmetry applies and the orientation of the unit vectors in spherical coordinates has been accounted for ($y$- and $z$-axis components are identical by symmetry).

## 4 NUMERICAL EXAMPLES

In this section we first demonstrate the feasibility of the multidomain approach for a homogeneous sphere. Snapshots and synthetic seismograms are then shown for a spherically symmetric model.

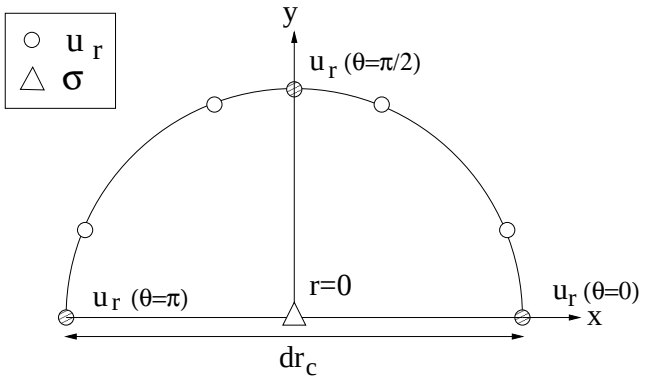


**Figure 5.** Treatment of the earth's centre in Cartesian form. The radial displacement has to be interpolated to the $x$- and $y$-axes (dashed circles). To evaluate the stress at $r=0$ the derivatives are taken along the $x$ and $y$ coordinates using the radial displacements. See text for details.

### 4.1 Homogeneous model

An important test of whether the wavefield is propagated accurately through the boundaries of domains with different grid spacing is a homogeneous model. Our homogeneous model is described by eight domains, with the top domain defined on a $1024\times256$ grid. The number of gridpoints along both axes is halved from one domain to the next deeper one. The radial grid spacing is $\approx$12 km. The arc length of the lateral grid spacing ranges from 22 km (the earth's surface) to 6 km (near the earth's centre). The time step is 0.25 s.

Two snapshots for $P$ waves emanating from an explosive point source in a liquid sphere with $P$ velocity 10 km s$^{-1}$ are shown in Fig. 6. The wavefield is shown above 0.5 per cent of its maximum value. There are virtually no artificial reflections or signals from either the domain boundaries or the earth's centre visible. This gives us confidence that we can use this approach for realistic earth models.

### 4.2 PREM

We now simulate wave propagation through the spherically symmetric PREM model (Dziewonski & Anderson 1981). The crust and ocean layers are left out and mantle properties extended to the earth's surface. The source is an explosion at the earth's surface. The grid size at the top of the model is $3200\times400$. The time step is 0.09 s. 16 700 time steps are evaluated to give a total record length of $\approx$1500 s. Snapshots of the pressure field are shown in Fig. 7. The dominant period is 20 s. The greyscaling was chosen to allow us on the one hand to see the continuation of the individual phases and on the other to highlight differential amplitudes. The energy is large where the wavefield is dark.

Such a grid set-up leads to a total number of $\approx$2 million gridpoints. The executable requires 105 Mbyte. On a symmetric hardware architecture with a maximum of eight processors (DEC 8400-5/625) and a clock speed of 625 MHz the simulation time is 640 min on one processor and 88 min on eight processors. Note the efficient speed-up of this application by a

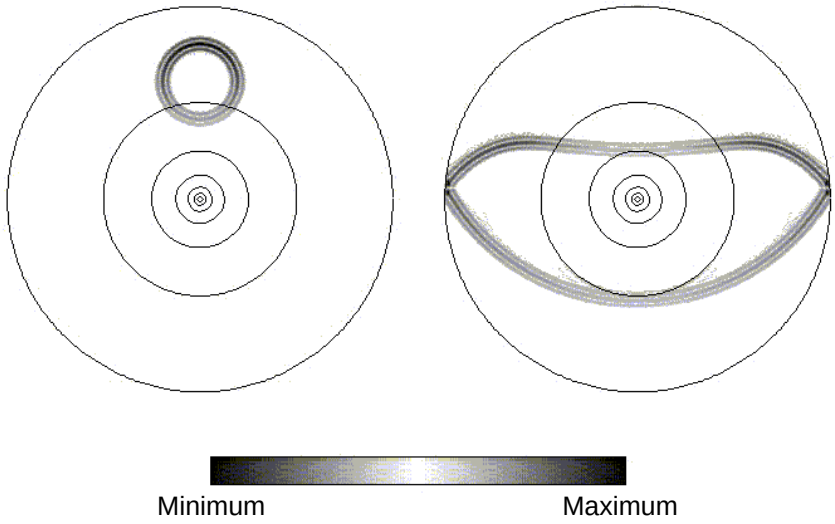


**Figure 6.** Snapshots of wave propagation through a homogeneous model ($v_p = 10$ km s$^{-1}$) for a source at 2000 km depth. The domains with different lateral grid spacing are indicated. The wavefield is shown above 0.5 per cent of its maximum value. There are virtually no artificial reflections or signals from either the domain boundaries or the earth's centre visible.

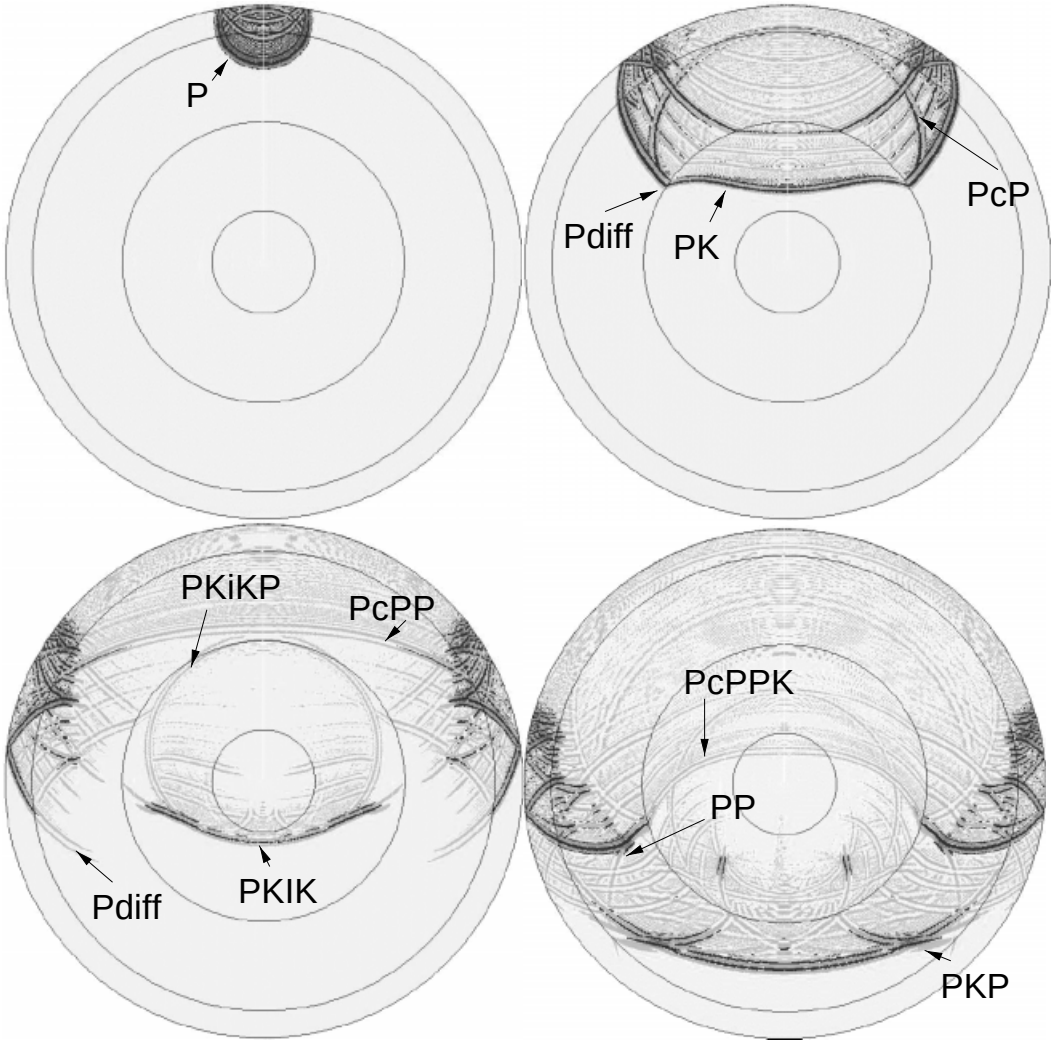


**Figure 7.** Snapshots of *P*-wave propagation through PREM for a source at the surface. The dominant period is 20 s. The greyscaling has been chosen to allow visualization of most of the phases and also to describe amplitude effects. The energy is large in the dark regions of the wavefield. Top left: *P* wavefield after 150 s; top right: after 450 s; bottom left: after 750 s; bottom right: after 1050 s. The discontinuities indicated are the 670 km discontinuity, the core–mantle boundary and the inner core boundary. Some of the dominant phases are marked.

factor of 7.3 through parallelization using high-performance Fortran exploiting the data-parallel structure of the algorithm.

The snapshots indicate the great complexity of the *P* wavefield inside the earth, even without the interaction with shear waves. In the first snapshot (Fig. 7, top left) the direct wave (*P*) propagating downwards can be identified. The smaller phases trailing the direct wave (visible in all snapshots) are caused by the upper mantle discontinuities. They were also observed in *SH* snapshots (Igel & Weber 1995).

In the second snapshot (Fig. 7, top right) the direct wave has entered the outer core and the core–mantle boundary (CMB) reflection (*PcP*) can be seen propagating upwards. Note the increasing complexity of the near-surface wavefield caused mainly by multiple surface reflections (*PP*, *PPP*, etc.). The slower velocities in the outer core lead to the change in wavefield curvature across the CMB (e.g. *PK*).

In the third snapshot (Fig. 7, bottom left) we can see the direct wave exiting the inner core (*PKIK*) and the reflection at the inner-core boundary (*PKiKP*) propagating upwards. The leading wave front propagating through the outer core is beginning to dominate over the (decaying) direct wave front in the mantle (shadow zone, Fig. 7, bottom right). The *PKP* triplication is forming in the mantle, leading to strong constructive interference and thus energy in the *PKP* phase, which is the first (significant) wave to arrive at epicentral distances greater than 140° (Fig. 7, bottom right). There is controversy about the origin of precursory phases observed at this distance range. The application of the approach presented here deals with this issue in such a way that we test many different parameters of scatterers in the lower mantle that cause precursor phases to *PKPdf*.

### 4.3 Synthetic seismograms

We first compare seismograms calculated with the algorithm presented in this paper with previously published and verified solutions. Fig. 8 shows the vertical displacements recorded at 45° epicentral distance for a dominant period of 35 s (source depth 200 km). Displacements are calculated with an elastic algorithm (Igel & Weber 1996) where the shear modulus was set to zero (i.e. an acoustic model) and with the acoustic multidomain approach. There is good agreement between the two solutions, the difference being below 0.5 per cent (relative energy).

Synthetic seismograms (pressure) recorded at the earth's surface with a receiver distance of 5° are shown in Fig. 9. The dominant period in the seismograms is 10 s and the cut-off period is 4 s. The source depth is 200 km. Ray-theoretical arrival times for *P*, *PP* and *PKP* phases are plotted on top of the seismograms, indicating the accuracy of the arrival times of the numerical calculations. Note the rapid decrease in amplitude of the diffracted *P* wave (and the corresponding depth phase) at around 100°, making the *PKP* phase the first significant arrival at large epicentral distances.

The interference of the various branches of the *PKP* and *PKIKP* phases at around 150° leads to the large amplitudes observed at these distances. This is further highlighted in Fig. 10, where pressure seismograms for a dominant period of 20 s are shown between 130° and 160°. Again the ray-theoretical arrival times have been superimposed. The individual *PKP* branches can be identified clearly.

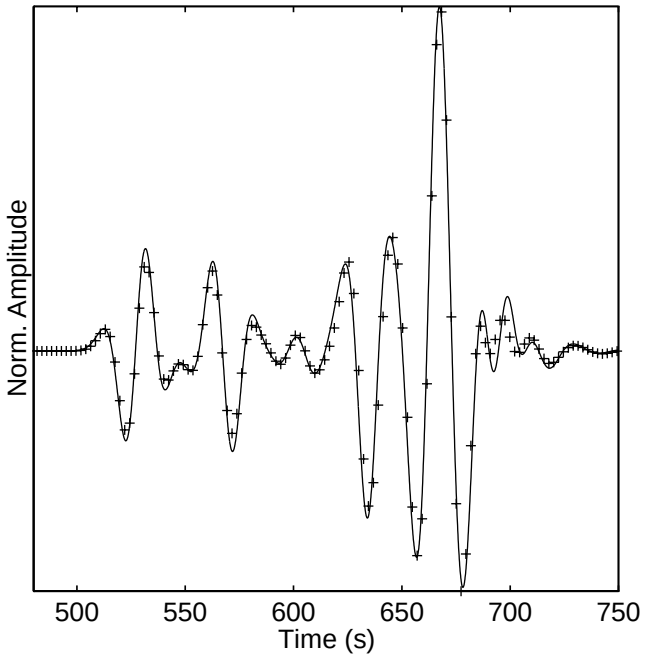


**Figure 8.** Comparison of the acoustic algorithm presented in this paper (+) with the elastic algorithm (solid line, Igel & Weber 1996), where the shear modulus has been set to zero. The receiver distance is 45°. The model is PREM, the source depth is 200 km and the dominant period is 35 s.

Precursory waves in this distance range have been observed in many other studies (reviewed in e.g. Thomas *et al.* 1999), and several causes for their origin have been given. Our algorithm allows us to model the complete wavefield—at least in the acoustic approximation—and to investigate the effects of heterogeneities in the lowermost mantle on the *PKP* phase. In particular, we can consider mechanisms for generating scattered energy that arrives prior to the *PKP* phase.

## 5 MODELLING PRECURSORS

To study the influence of scatterers in the lower mantle on the wavefield of *PKP*, we compute models with different kinds of scatterers. The reference earth model is PREM (Dziewonski & Anderson 1981). The source is at a depth of 192 km and the receivers are at an epicentral distance of 130–150° in 0.25°

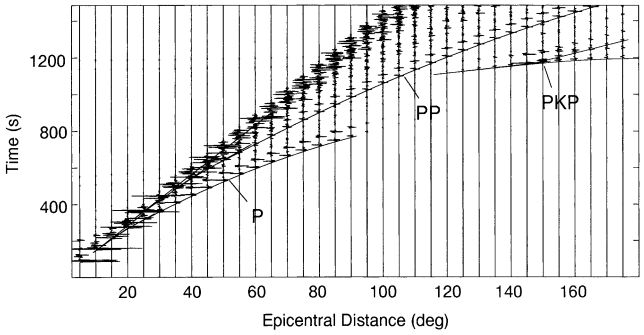


**Figure 9.** Seismograms through PREM for a source depth of 200 km. The dominant period is 10 s. The ray-theoretical arrival times of *P*, *PP* and *PKP* are indicated.

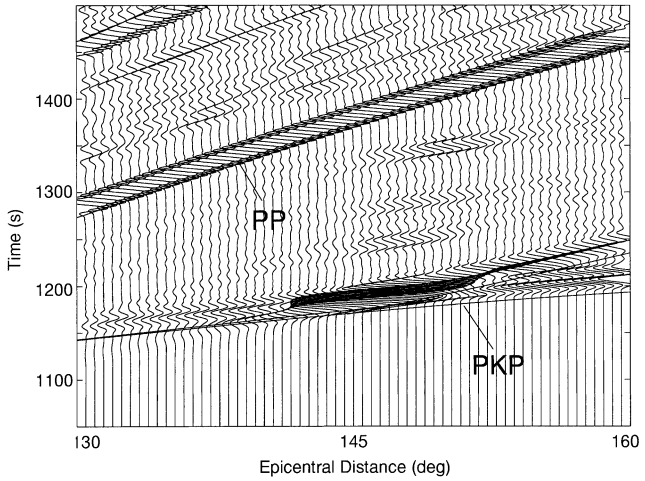


**Figure 10.** Seismograms through PREM for a surface source. The dominant period is 20 s. The seismograms are shown at epicentral distances where we expect the triplication of the *PKP* branches. The ray-theoretical arrival times of *PP* and *PKP* are indicated. Note the strong constructive interference at $\approx 145^\circ$.

steps. Fig. 11 shows the different model configurations used to investigate the influence of velocity contrast, orientation and location of scatterers on the *PKP* wavefield.

Scatterers with various velocity contrasts have been placed at different locations in the lower mantle. Velocity contrasts of the scatterer between $-30$ per cent and +30 per cent have been modelled. The location of the scatterer varies between 116 and 133° from the source (that is, between 24° and 7° from the centre of the receiver array). The size of the scatterer is 200 km in height and 3° in width (about 180 km at the CMB). In addition, a model with two scatterers at the CMB and a model with one scatterer 500 km above the CMB have been studied.

Use of the acoustic approximation is appropriate for studying *PKP* precursors because we are interested mainly in geometric scattering effects of *P* waves in the lower mantle. Conversions from *P* to *S* at the scatterer would have a much longer traveltime. If no *P*-to-*S* conversions are considered, the amplitudes of both the precursor and the main phases will be higher than with conversions. Therefore, we can study the slowness and traveltime effects of scatterers on *PKP* but no quantitative studies can be made for the amplitude. Due to the rotational symmetry, the scatterers in our models become 'doughnut-shaped' scatterers. However, off-path scattering would produce phases that would arrive after phases produced by scattering on the great-circle path. Also, these ring-like scatterers most probably produce different spreading from a 3-D scatterer.

It has been shown that different orientations of scatterers can produce different precursor signals (Cormier 1999). Therefore, we also placed scatterers at the bottom of the earth's mantle with aspect ratios of $\sim 4:1$ and $2:1$, respectively, in two different orientations and two different velocity contrasts.

Another model we used is a global ultra-low-velocity layer (ULVZ) at the base of the mantle. ULVZs have been discovered in different regions at the bottom of the earth's mantle (e.g. Garnero & Helmberger 1995). The (global) ULVZ in our model has a height of 300 km and a velocity contrast of $-10$ per cent. Also, a global ULVZ with a thin scatterer at either the source or the receiver side has been studied. The velocity contrast of the scatterers within the ultra-low-velocity layer is $+10$ per cent compared to the reference model PREM (i.e. $+22$ per cent compared to the ULVZ). To study the effect of an ultra-high-velocity layer, (e.g. $D''$), a 300 km thick global layer was placed at the CMB with a velocity contrast of $+10$ per cent.

Since it is not yet possible to compute synthetic waves with a period of 1–2 s, we study the effect of our models on long-period data (dominant periods of 11 s). This is the reason to choose a scale length of our scatterers up to 200–300 km. The

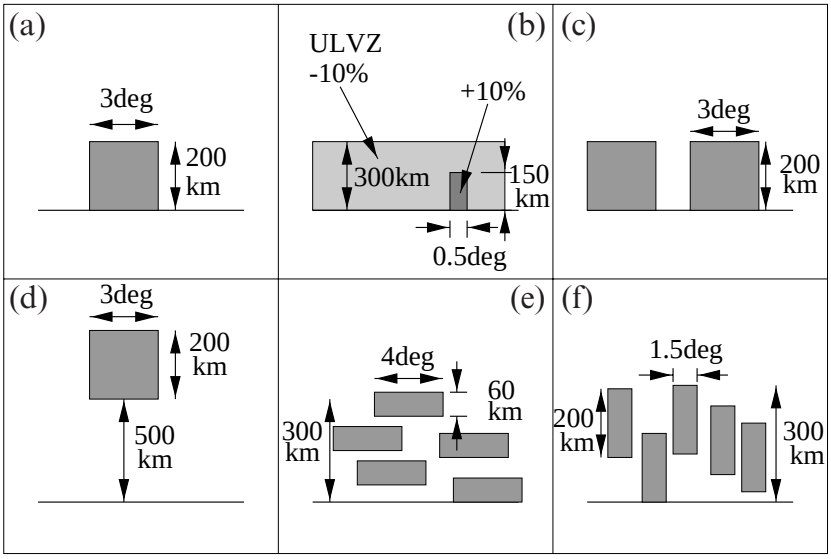


**Figure 11.** Models of scatterers that have been used to study the effect on the *PKP* wavefield. (a) A box, 3° in width and 200 km in height, with various velocity contrasts at the CMB. (b) An ultra-low-velocity layer at the base of the mantle (height: 300 km) either with or without a thin (0.5°) scatterer at the receiver side. (c) Two scatterers (size as in a) at the CMB. (d) A scatterer (size as in a) 500 km above the CMB. (e) Five scatterers in a horizontal orientation with an aspect ratio of about 4 : 1 within the lowest 300 km of the mantle. (f) As (e) but in a vertical orientation and with an aspect ratio of 2 : 1.

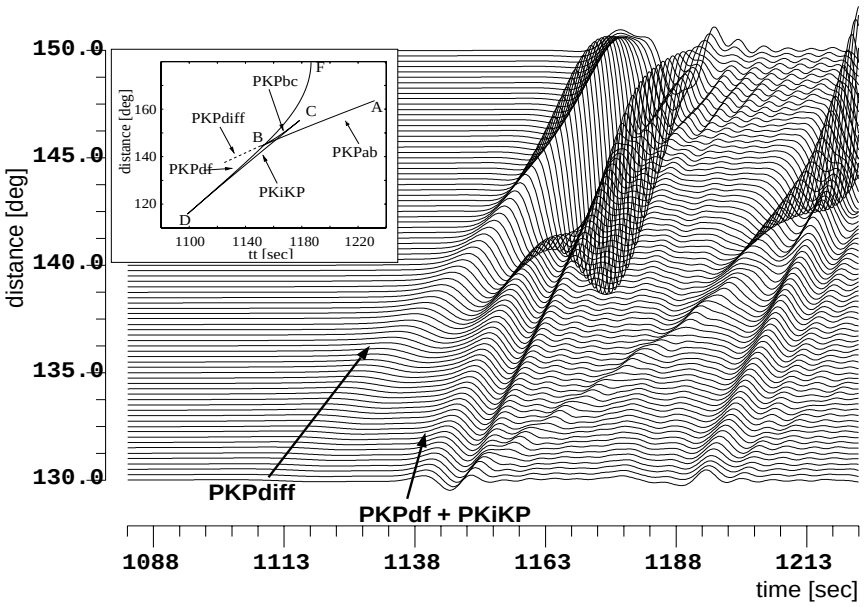


**Figure 12.** A seismogram section of (FD) synthetic seismograms (pressure) for model PREM with a traveltime curve for *PKP*. The phase ahead of *PKPdf* and *PKiKP* with a similar slope as *PKPab* at the cusp point is a diffracted wave due to the long periods of the synthetics ($PKP_{\mathrm{diff}}$). The seismogram traces were filtered with a low-pass filter (11 s, order of filter: 2). The receiver array is at an epicentral distance of 130°–150° in 0.25° steps. A two-sided wavelet is used.

scale length of the scatterers found from the analysis of short-period filtered data, however, is between 8 and 20 km (Hedlin *et al.* 1997; Cormier 1999). The scale lengths of scatterers found from long-period scattered *PKP* waves (Wen & Helmberger 1998a) is 100–300 km vertically and 60–80 km in height, compatible with the synthetic models we are investigating.

## 6 RESULTS OF MODELLING PRECURSORS

### 6.1 PREM

Using a model without scatterers (PREM), only standard phases such as the direct *P* wave, *P* reflections, *P* diffracted waves or the four different branches of *PKP* should be visible. Fig. 12 shows a synthetic seismogram section (pressure) for stations at epicentral distances of 130–150° with 0.25° spacing. The four branches of *PKP* can be seen together with the diffracted *PKP* wave from the B-caustic at distances smaller than 144°. For short-period data (1 Hz) the diffracted *PKP* wave should not be seen at epicentral distances of 143° or shorter (e.g. Bataille *et al.* 1990). A vespagram (Davies *et al.* 1971) was produced using seismogram traces at an epicentral distance between 132 and 140° (Fig. 13). The distance range was chosen in order to avoid the large amplitudes at and beyond the caustic (at 144° at the surface) and most of the diffracted *PKP* wave. Fig. 13 shows again the standard phases *PKPdf* and *PKiKP*, which overlap due to the long periods (dominant periods of 11 s). Ahead of *PKPdf* the diffracted *PKP* wave can be seen. $PKP_{\mathrm{diff}}$ appears to be two phases due to the contributions of different slowness values from the two branches (*ab* and *bc*) at larger distances. A verification of the results for PREM without scatterers was made using the reflectivity method (Müller 1985).

Using vespagrams it becomes possible to distinguish between a diffracted wave and a scattered wave since the slowness and the traveltime of the phases can be determined.

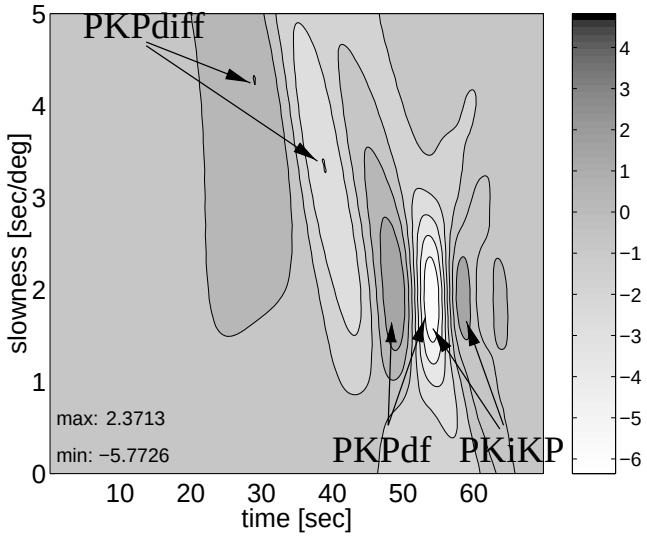


**Figure 13.** Linear vespagram for a synthetic seismogram section for model PREM without scatterers using traces at a distance range between 132° and 140°. The energy of *PKPdf* and *PKiKP* branches can be seen, with the corresponding slowness values of 1.8 s/° and 2 s/°, respectively. Energy ahead of *PKPdf* is $PKP_{\mathrm{diff}}$. The greyscale gives amplitude in arbitrary units and is chosen to be the same in all the following vespagrams. Maximum and minimum amplitudes of the stacked traces are given in the bottom left corner.

### 6.2 PREM with scatterer

If a scatterer is placed in the lower mantle or at the CMB, an additional phase arrives in the time window ahead of *PKPdf*. This additional phase can be seen in both seismograms (Fig. 14) and vespagrams (Fig. 15). Since it is difficult to analyse the effects of a scatterer in a standard vespagram due to the

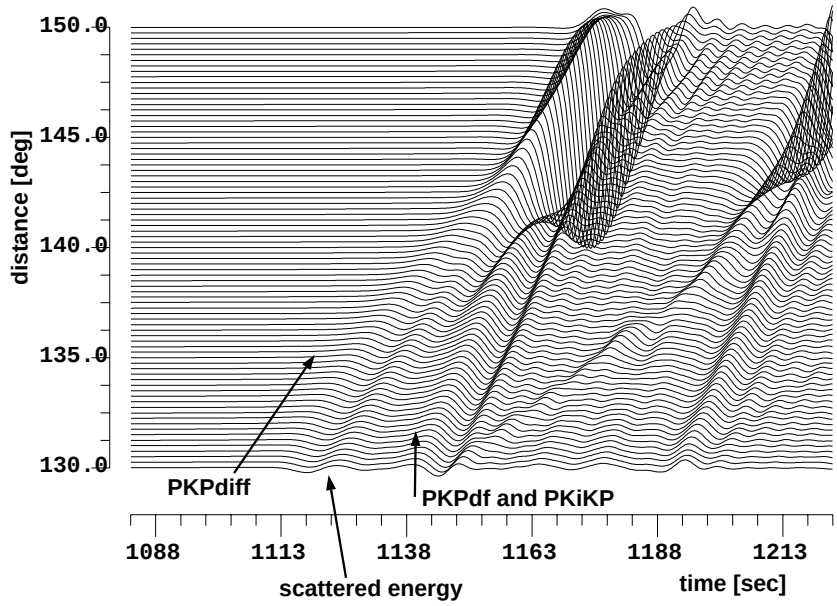


**Figure 14.** Synthetic seismogram section as in Fig. 12 but for PREM with a scatterer at an epicentral distance of 116°–119° at the CMB with a velocity contrast of +10 per cent (model shown in Fig. 11a). Energy between $PKP_{diff}$ and *PKPdf* can bee seen with a different slope as *PKPdf* which is due to the scatterer.

long periods of the data and overlapping of phases, residual vespagrams were produced (Fig. 16). The traces of the seismogram for model PREM (Fig. 14) are subtracted from the model with scatterer (Fig. 12). A vespagram is then produced using the residual seismogram traces. In these residual seismograms only the effects of scatterers are visible. Using residual vespagrams it is also possible to demonstrate the influence of the scatterer on the *PKP* waveform. The phase in Fig. 16 is a scattered phase with a traveltime about 10 s faster than that of *PKPdf* and a slowness of ~3 s/°. Since we are using a two-sided wavelet for *P*, the scattered wave also appears as a two-sided wavelet. In the following section we will analyse only residual vespagrams to study the effects of different parameters of scatterers.

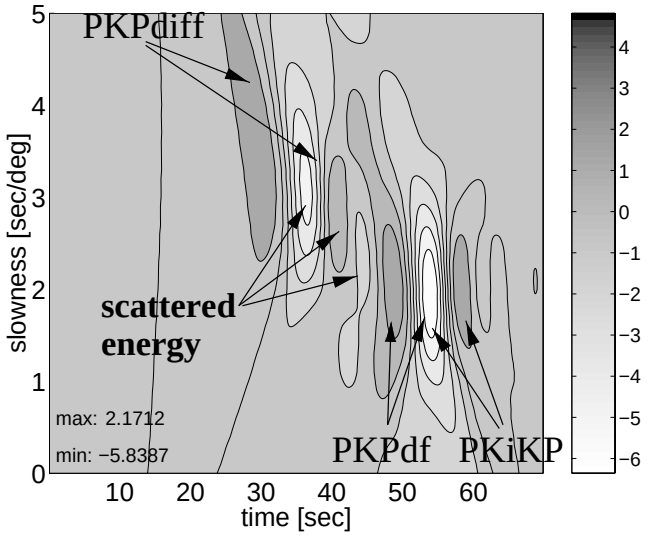


**Figure 15.** Linear vespagram for the synthetic seismogram section in Fig. 14 using traces at a distance range between 132° and 140°. The scattered wave interferes with *PKP* and is therefore difficult to analyse.

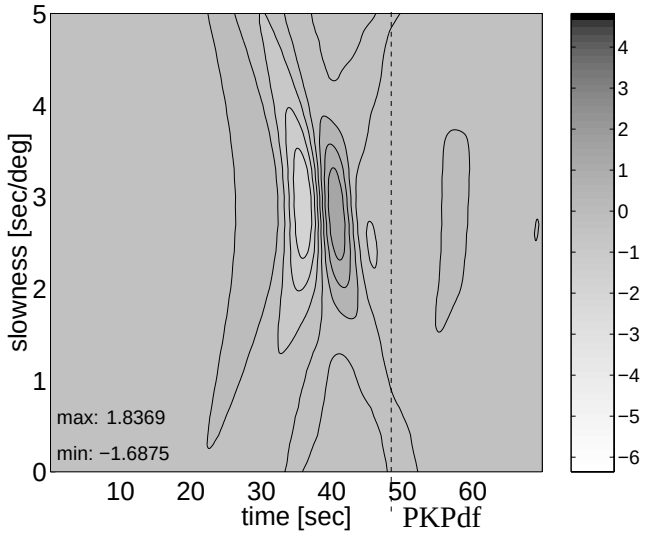


**Figure 16.** Residual vespagram of a residual seismogram section (seismogram traces of model with scatterer − seismogram traces of PREM). The phase seen is due to the scatterer. Maximum and minimum amplitude are indicated in the bottom left corner. The scattered wave arrives about 10 s ahead of *PKPdf* with a slowness of 3 s/°. As a reference, the *PKPdf* arrival time for model PREM (first maximum) is indicated by the dashed line. The amplitude of the scattered phase in the distance range between 132° and 140° in Fig. 14 (left) is about 30 per cent of the *PKPdf* amplitude in this distance range.

### 6.3 Influence of different parameters of scatterers

The effects of different parameters of scatterers on *PKP* and scattered waves will be described in this section. Scatterers at both the source side and the receiver side produce precursor arrivals. In the following we study only the effect of receiver-side

| **Influence of scatterer** | | **Effect on precursor** | | | |
|---|---|---|---|---|---|
| | | amplitude | slowness | travel time | waveform |
| location | | first increases then decreases again w. larger epic. dist. | decreasing with increasing epic. distance | increasing with increasing epic. distance | —— |
| velocity contrast | | larger for increasing vel. contrast (min. 5%) | smaller for neg. contrast higher for pos. contrast | longer for neg. contrast shorter for pos. contrast | reversed between pos. and neg. contrast. |
| depth | | effect on scattered energy small<br>scatterer above CMB has an influence on PKP-wavelet | | | |
| number of scatterers | | wavefield more complex compared to one scatterer<br>interference of precursors possible (maybe multiple scattering) | | | |
| orientation (5 scatterers) | hor. | 5 scatterers have same effect as one large scatterer | | | |
| | vert. | precursor wavefield more complex (as described above)<br>smaller amplitude compared to horiz. oriented scatterers<br>slowness values between 2 and 3 sec/deg for the model studied | | | |
| ULVZ, UHVZ | | no energy in time window where precursors are expected | | | |

**Figure 17.** The effects of different parameters of scatterers on amplitude, slowness, traveltime and waveform of precursors.

scatterers. Fig. 17 summarizes the effects of location, velocity contrast, orientation, number of scatterers and an ULVZ and UHVZ.

The location has an influence on the amplitude, the slowness and the traveltime of the scattered phase. If the scatterer is moved towards greater epicentral distance the amplitude of the scattered phase first increases and then decreases again from a certain distance. This defines a precursor envelope that is similar to the amplitude behaviour discussed by Hedlin *et al.* (1997) and Vidale & Hedlin (1998). The slowness of the scattered phase decreases from 3.0 s/° to 2.1 s/°. For greater epicentral distances the traveltime of the scattered phase increases, that is, the scattered wave arrives closer to *PKPdf* than for smaller epicentral distances. The effects of different locations on amplitude, traveltime and slowness are summarized in Fig. 18.

To study the effect of the depth of a scatterer and, if possible, to find a criterion to distinguish between a scatterer at and above the CMB, scatterers have been placed at different depths in the mantle (models given in Figs 11a and d). The location of the scatterer depends on the *PKPab* path since scattering at the receiver side occurs if the *PKPab* wave interacts with small-scale inhomogeneities. The vespagrams for both models look similar for the scattered phase ahead of *PKPdf* (Figs 19a and b). Both traveltime and slowness differ only slightly, which may be due to slightly different locations of the scatterers on the *PKPab* path. The amplitude of the precursor in Fig. 19(b) (500 km above the CMB) is smaller than for the model with a scatterer at the CMB. The most obvious difference, however, between a scatterer at the CMB and a scatterer above the CMB is the influence of the scatterer on *PKPdf* and *PKiKP*. The reason for this is that the scatterer interacts with *PKP* on the *PKPab* path as well as on the *PKPdf* path because both paths are close to each other at a depth of 500–800 km above the CMB (see also Fig. 1).

If two scatterers are placed at the CMB (model shown in Fig. 11c), the precursor wavefield becomes more complex (Fig. 20). Due to the different location of the scatterers at the CMB, the precursors have different slownesses and traveltimes and therefore can interfere, which produces a precursor wavefield comparable to the precursor wavefield seen in real data.

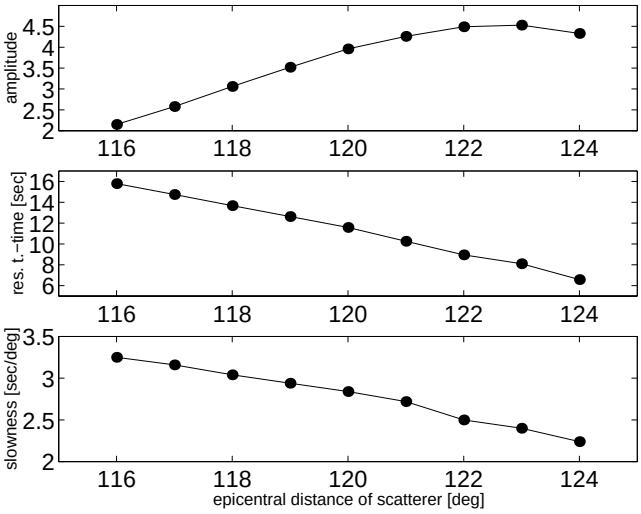


**Figure 18.** The effects of location of one scatterer at the CMB (model given in Fig. 11a) on amplitude of the corresponding precursor, the residual traveltime between *PKPdf* and the precursor and slowness of the precursor. The residual traveltime was measured between the first maximum of the precursor and *PKPdf* in differential vespagrams. The errors are 1 s for traveltime and 0.1 s/° for slowness. The amplitude is given in arbitrary units.

Since scattering occurs in regions where the velocity is faster as well as in regions where the velocity is slower compared to the average velocity in tomographic models (e.g. van der Hilst *et al.* 1997; Grand *et al.* 1997), we study the influence of different velocity contrasts. To produce visible precursors to *PKPdf*, a velocity contrast of at least $\pm 5$ per cent is required. The differences in slowness and traveltime vespagrams for

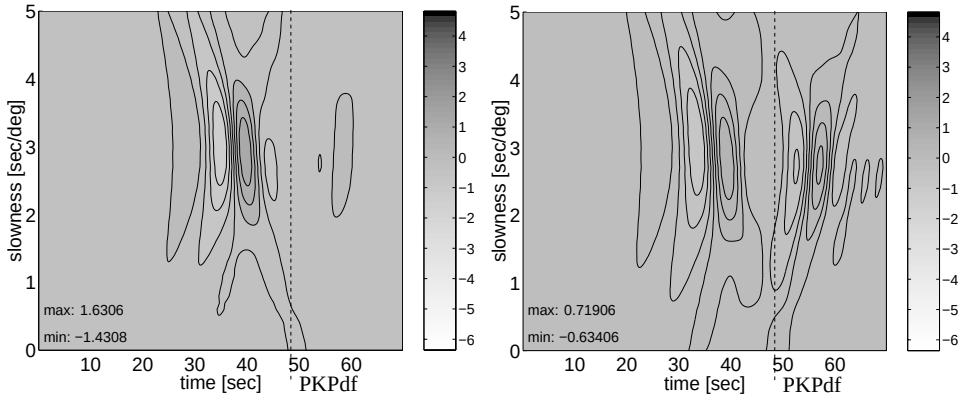


**Figure 19.** (a) Residual vespagram for a model with a scatterer at the CMB at a distance 118°–121° from the source and a height of 200 km (model in Fig. 11a). The velocity contrast is +10 per cent. *PKPdf* arrival time (first maximum) for PREM is indicated by the dashed line. (b) As (a) but for a scatterer 500 km above the CMB at an epicentral distance of 123°–126° with a velocity contrast of +10 per cent (model in Fig. 11d).

either positive (+20, +10 and +5 per cent) or negative contrasts (−20, −10 and −5 per cent) are small. The difference between positive and negative contrasts is stronger: a scatterer with a negative contrast produces a precursor with a longer traveltime than a scatterer with a positive contrast. The slowness for precursors also differs slightly (smaller for negative contrasts) and the polarity of the precursors is reversed in vespagrams for positive and negative contrasts of scatterers. Fig. 21 summarizes the effects of velocity contrast of a scatterer on amplitude, traveltime and slowness of the precursor.

Studying five scatterers in different orientations (models given in Figs 11e and f), it turned out that the precursor wavefield is more complex than for only one scatterer, especially for scatterers in a vertical orientation. This effect, which is due to the larger number of scatterers, was discussed above. Horizontally oriented scatterers do not have as strong an effect as vertically oriented scatterers since the horizontally elongated scatterers act as one single large scatterer for the periods of synthetic waves used in this study.

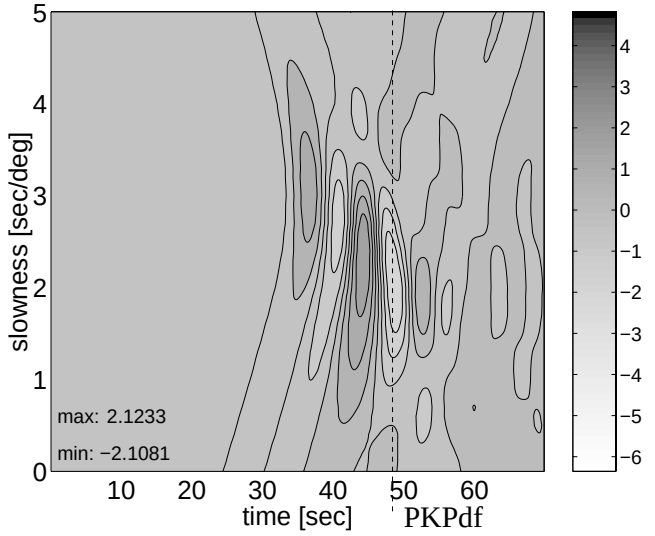


**Figure 20.** Residual vespagram for a model with two scatterers at the CMB (at 118°–121° and 124°–127° from the source, height of scatterers 200 km and velocity contrast of −10 per cent). The dashed line indicates the *PKPdf* arrival time (first maximum) for PREM.

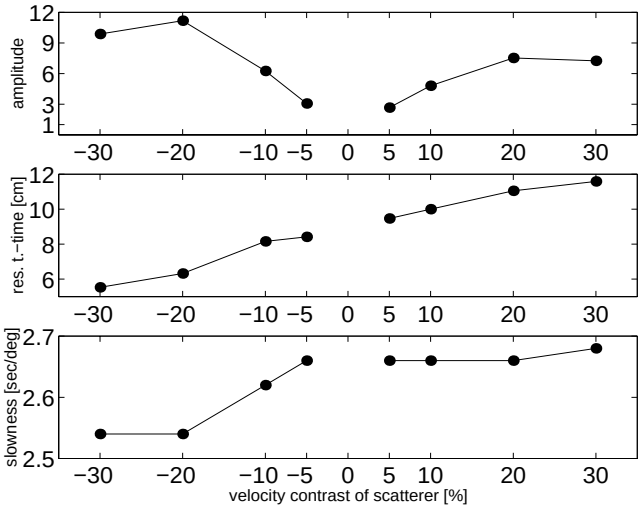


**Figure 21.** The effects of velocity contrast of a scatterer on amplitude of the corresponding precursor, the residual traveltime between *PKPdf* and the precursor and slowness of the precursor. The residual traveltime was measured between the first maximum of the precursor and *PKPdf* in differential vespagrams. The errors are 1 s for traveltime, 0.1 s/° for slowness. Amplitude values are given in arbitrary units.

A model with a global ULVZ or UHVZ is not able to produce arrivals in the time window where precursors are usually expected. If a small scatterer is placed within the ULVZ at the receiver side (model shown in Fig. 11b), a precursor arrives in the time window of 25 s ahead of *PKPdf*. This precursor wave, however, is due to the scatterer, as described above.

## 7 DISCUSSION AND CONCLUSIONS

While numerical modelling of wave propagation through heterogeneous media has been widely applied in exploration seismology, only recently have various numerical techniques been used to solve wave propagation problems on a global scale. The reason is that on a global scale a complete solution to the wave equation is computationally expensive, in particular when short spatial wavelengths in the medium and in the wavefield are to be modelled. However, with the advent of

parallel hardware, modelling on a planetary scale of many geophysical processes such as mantle convection, the Earth's magnetic field and seismic wave propagation has become feasible.

In global seismology the problem can be addressed in many different ways. Traditionally forward solutions have been built around the normal mode approach exploiting the spherical symmetries of the Earth's heterogeneities. Whilst the complete wavefield can be simulated for spherically symmetric structures, perturbation techniques are required for general 3-D structures to make the problem solvable. However, strong and particularly discontinuous lateral heterogeneities such as subduction zones are difficult to describe with the normal mode approach. Ray-based methods are not able to model diffracted phases accurately and therefore are not applicable in the general case.

Standard numerical methods used in Cartesian systems such as the finite difference method are not easily applied in curvilinear systems containing coordinate singularities. In this paper we suggest an algorithm that allows the wave equation to be solved for the whole sphere using the finite difference method. We employ a multidomain approach, thereby considerably reducing the required simulation length for a given problem. Furthermore, with our technique waves can propagate through the centre of the Earth without experiencing the coordinate singularity. This is an improvement over earlier algorithms (e.g. Igel & Weber 1996; Furumura *et al.* 1998) where the physical domain had to terminate at a certain depth level and absorbing boundary conditions needed to be applied.

The frequency range that can be achieved today (dominant periods down to 10 s) and the fine grid sampling that is possible (a few kilometres) implies that we will soon be able to investigate high-frequency effects of medium- and short-scale heterogeneities inside the Earth on globally recorded signals without the approximations previously necessary. This should allow us to improve the resolution of our structural imaging of the Earth's interior.

Using the algorithm presented in this paper, we have studied some of the mechanisms that can produce precursors to *PKPdf*, often seen in data at epicentral distances between 125° and 143° (e.g. Haddon & Cleary 1974; Vidale & Hedlin 1998; Wen & Helmberger 1998a). For example, scatterers in a horizontal or vertical orientation have different effects on precursors. One possibility for vertically elongated scatterers can be plumes or plume-like structures (that is, vertical temperature perturbations) (e.g. Stacey & Loper 1983). Horizontally elongated scatterers could be formed by low-velocity layers (e.g. Garnero & Helmberger 1998) or subducted slabs that have penetrated into the lower mantle and remain at the base of the mantle (e.g. Christensen & Hofmann 1994).

We have investigated the influence of velocity contrasts, location and orientation on precursors to *PKPdf*. Using residual vespagrams it is possible to find differences in slowness and traveltime of scattered waves caused by different parameters of scatterers (velocity contrast, location, etc.). It has turned out that by changing the parameters of a scatterer, the traveltime, amplitude and slowness of the scattered phase are influenced and different combinations of parameters can result in scattered phases that are alike. Moreover, some scatterers at certain locations also have an influence on the *PKP* wavelet. Since the FD scheme is carried out for rotationally symmetric media, it is not possible to study the influence of out-of-plane scatterers. The azimuth has been shown to have a strong influence on traveltime and slowness of the scattered phase (e.g. Thomas *et al.* 1999). This gives another free parameter for the explanation of the precursor coda. In conclusion, this parameter study has shown that due to many different parameters of scatterers such as location, velocity contrast, orientation and depth, it is not possible to find a unique set-up to produce precursor wavefields as seen in real data, at least not with the periods used in this study. The same precursor wavefield can be produced by a variety of different model set-ups. It could be that for short-period synthetic data the differences between the models are more prominent than for long-period synthetic data. Combined theoretical methods as described by Wen & Helmberger (1998b) can possibly help to distinguish between different parameters since these methods can also be used for short-period data.

## ACKNOWLEDGMENTS

We gratefully acknowledge the Enigma Project at the Institute of Theoretical Geophysics in Cambridge for access to their computational facilities (DEC 8400-5/625). Thanks to Torsten Dahm for helpful comments. This research was partly supported by grant GR3/10086 of the National Environmental Research Council (HI) and also through the German Research Foundation (HI, Heisenberg fellowship; CT, PhD grant). Thanks to three anonymous reviewers and Michael Korn for constructive comments.

## REFERENCES

Alterman, Z., Aboudi, J. & Karal, F.C., 1970. Pulse propagation in a laterally heterogeneous solid elastic sphere, *Geophys. J. R. astr. Soc.,* **21,** 243–260.

Bataille, K., Wu, R.-S. & Flatté, S.M., 1990. Inhomogeneities near the core-mantle boundary; evidence from scattered waves: a review, *Pure appl. Geophys.,* **132,** 151–173.

Chaljub, E. & Tarantola, A., 1997. Sensitivity of SS precursors to topography on the upper-mantle 660-km discontinuity, *Geophys. Res. Lett.,* **24,** 2613–2616.

Christensen, U.R. & Hofmann, A.W., 1994. Segregation of subducted oceanic crust in the convecting mantle, *J. geophys. Res.,* **99,** 19 867–19 884.

Cleary, J.R. & Haddon, R.A.W., 1972. Seismic wave scattering near the core-mantle boundary: a new interpretation of precursors to PKP, *Nature,* **240,** 549–551.

Cormier, V.F., 1999. Anisotropy of heterogeneity scale lengths in the lower mantle from *PKIKP* precursors, *Geophys. J. Int.,* **136,** 373–384.

Cummins, P.R., Geller, R.J., Hatori, T. & Takeuchi, N., 1994a. DSM complete synthetic seismograms: SH, spherically symmetric case, *Geophys. Res. Lett.,* **21,** 533–536.

Cummins, P.R., Takeuchi, N., Geller, R.J. & Hatori, T., 1994b. DSM complete synthetic seismograms: P-SV, spherically symmetric, case, *Geophys. Res. Lett.,* **21,** 1663–1666.

Cummins, P.R., Takeuchi, N. & Geller, R.J., 1997. Computation of complete synthetic seismograms for laterally heterogeneous models using the Direct Solution Method, *Geophys. J. Int.,* **130,** 1–16.

Davies, D., Kelly, E.J. & Filson, J.R., 1971. Vespa process for analysis of seismic signals, *Nature Phys. Science,* **232,** 8–13.

Doornbos, D.J. & Vlaar, N.J., 1973. Regions of seismic wave scattering in the Earth's mantle and precursors to PKP, *Nature Phys. Sci.,* **243,** 58–61.

Dziewonski, A. & Anderson, D.L., 1981. Preliminary reference Earth model, *Phys. Earth planet. Inter.,* **25,** 297–356.

Falk, J., Tessmer, E. & Gajewski, D., 1996. Tube wave modelling by the finite-difference method with varying grid spacing, *Pure appl. Geophys.,* **148,** 77–93.

Furumura, T., Kennett, B.L.N. & Furumura, M., 1998. Seismic wavefield calculation for laterally heterogeneous whole earth models using the pseudospectral method, *Geophys. J. Int.,* **135,** 845– 860.

Garnero, E.J. & Helmberger, D.V., 1995. A very slow basal layer underlying large-scale low-velocity anomalies in the lower mantle beneath the pacific: evidence from core phases, *Phys. Earth planet. Inter.,* **91,** 161–176.

Garnero, E.J. & Helmberger, D.V., 1998. Further structural constraints and uncertainties of a thin laterally varying ultralow-velocity layer at the base of the mantle, *J. geophys. Res.,* **103,** 12 495–12 509.

Geller, R.J. & Ohminato, T., 1994. Computation of synthetic seismograms and their partial derivatives for heterogeneous media with arbitrary natural boundary conditions using the Direct Solution Method, *Geophys. J. Int.,* **116,** 421–446.

Grand, S.P, van der Hilst, R.D. & Widiyantoro, S., 1997. Global seismic tomography: a snapshot of convection in the Earth, *Geol. Soc. Am. Today,* **7,** 1–7.

Haddon, R.A.W. & Cleary, J.R., 1974. Evidence for scattering of seismic PKP waves near the core mantle boundary, *Phys. Earth planet. Inter.,* **8,** 211–234.

Hedlin, M.A.H., Shearer, P.M. & Earle, P.S., 1997. Seismic evidence for small-scale heterogeneity throughout the Earth's mantle, *Nature,* **387,** 145–150.

Igel, H., 1999. Wave propagation in spherical sections by the Chebyshev spectral method, *Geophys. J. Int.,* **136,** 559–567.

Igel, H. & Gudmundsson, O., 1997. Frequency-dependent effects on amplitude and waveforms of S and SS waves, *Phys. Earth planet. Inter.,* **104,** 229–246.

Igel, H. & Ita, J., 1997. Teleseismic effects of subducting slabs: a numerical study, in *Upper Mantle Heterogeneity from Active and Passive Seismology,* pp. 333–341, ed. Fuchs, K., Kluwer, Dordrecht.

Igel, H. & Weber, M., 1995. SH-wave propagation in the whole mantle using high-order finite differences, *Geophys. Res. Lett.,* **22,** 731–734.

Igel, H. & Weber, M., 1996. P-SV wave propagation in the Earth's mantle using finite differences: application to heterogeneous lowermost mantle structure, *Geophys. Res. Lett.,* **23,** 415–418.

Igel, H., Mora, P. & Riollet, B., 1995. Anisotropic wave propagation through finite difference grids, *Geophysics,* **60,** 1203–1216.

Jastram, C. & Behle, A., 1992. Acoustic modelling on a grid of vertically varying grid spacing, *Geophys. Prospect.,* **40,** 157–169.

Jastram, C. & Tessmer, E., 1994. Elastic modelling on a grid with vertically varying spacing, *Geophys. Prospect.,* **42,** 357–370.

Kessler, D. & Kosloff, D., 1993. 3-D elastic simulation of wave propagation using cylindrical coordinates, *J. seism. Expl.,* **2,** 173–188.

King, D.W., Haddon, R.A.W. & Cleary, J.R., 1973. Array analysis of precursors to PKIKP in the distance range 128° to 142°, *Geophys. J. R. astr. Soc.,* **37,** 157–173.

Mozco, P., 1989. Finite-difference technique for *SH*-waves in 2-D media using irregular grids—application to the seismic response problem, *Geophys. J. Int.,* **99,** 321–329.

Müller, G., 1985. The reflectivity method: a tutorial, *J. Geophys.,* **58,** 153–174.

Stacey, F.D. & Loper, D.E., 1983. The thermal boundary layer interpretation of $D''$ and its role as a plume source, *Phys. Earth planet. Inter.,* **33,** 45–55.

Thomas, Ch., Weber, M., Wicks, C. & Scherbaum, F., 1999. Small scatterers in the lower mantle observed at German broadband arrays, *J. geophys. Res.,* **104,** 15 073–15 088.

van der Hilst, R.D., Widiyantoro, S. & Engdahl, E.R., 1997. Evidence for deep mantle circulation from global tomography, *Nature,* **386,** 578–584.

Vidale, J.E. & Hedlin, M.A.H., 1998. Evidence for partial melt at the core-mantle boundary north of Tonga from the strong scattering of seismic waves, *Nature,* **391,** 682–685.

Wen, L. & Helmberger, D.V., 1998a. Ultra low velocity zones near the core-mantle boundary from broadband PKP precursors, *Science,* **279,** 1701–1703.

Wen, L. & Helmberger, D.V., 1998b. A two-dimensional P-SV hybrid method and its application to modeling localized structures near the core-mantle boundary, *J. geophys. Res.,* **103,** 17 901–17 918.

Yoon, K. & McMechan, G.A., 1995. Simulation of long-period 3-D elastic responses for whole Earth models, *Geophys. J. Int.,* **120,** 721–730.